Quantum oscillations revealing topological band in kagome metal ScV_6Sn_6

Changjiang Yi,[1] Xiaolong Feng,[1] Ning Mao,[1] Premakumar Yanda,[1] Subhajit Roychowdhury,[1] Yang Zhang,[2,3] Claudia Felser,[1] and Chandra Shekhar[1,*]

[1]*Max Planck Institute for Chemical Physics of Solids, 01187 Dresden, Germany*

[2]*Department of Physics and Astronomy, University of Tennessee, Knoxville, Tennessee 37996, USA*

[3]*Min H. Kao Department of Electrical Engineering and Computer Science, University of Tennessee, Knoxville, Tennessee 37996, USA*

(Received 8 June 2023; accepted 15 December 2023; published 12 January 2024)

Compounds with kagome lattice structure are known to exhibit Dirac cones, flatbands, and van Hove singularities, which host numerous versatile quantum phenomena. Inspired by these intriguing properties, we investigate the temperature and magnetic field-dependent electrical transports along with the theoretical calculations of ScV_6Sn_6, a nonmagnetic charge-density wave (CDW) compound. At low temperatures, the compound exhibits Shubnikov–de Haas quantum oscillations, which help to design the Fermi-surface (FS) topology. This analysis reveals the existence of several small FSs in the Brillouin zone, combined with a large FS. Among them, the FS-possessing Dirac band is nontrivial and generates a nonzero Berry phase. In addition, the compound also shows the anomalous Hall-like behavior up to the CDW phase transition, and they might be correlated. Combining these interesting physical properties with the CDW phase, ScV_6Sn_6 presents a unique material example of the versatile $HfFe_6Ge_6$ family and provides various promising opportunities to explore the series further.

DOI: 10.1103/PhysRevB.109.035124

The kagome lattice gives rise to unavoidable exotic topological electronic states, namely Dirac point [1,2], van Hove singularity [3,4] and flatband [1,2]. These features have been extensively studied by different spectroscopy experiments in various kagome compounds. Depending on band filling and interactions, they accommodate a number of unconventional quantum phases, topological band structure [5–7], Chern insulator [8], unconventional superconductivity [9,10], and charge-density wave (CDW) [11–14]. The profound impacts of the kagome lattice have recently been highlighted by the discovery of CDW below 90 K in nonmagnetic AV_3Sb_5 and antiferromagnetic hexagonal-FeGe [11]. The charge orders in these systems are distinct. In AV_3Sb_5 [14–18], it is chiral, whereas in FeGe [11,19] magnetism is mediated. Similar to AV_3Sb_5 and FeGe, the CDW transition temperature (at 92 K) was recently discovered in the ScV_6Sn_6 compound [20]. ScV_6Sn_6 is the only known compound from the vast hexagonal $HfFe_6Ge_6$ family to exhibit a CDW phase transition, which is a first-order-like transition with propagation vector (1/3, 1/3, 1/3) revealed by early x-ray and neutron experiments [20]. The strongly coupled out-of-plane lattice dynamics suggests an unconventional nature of the CDW phase, which is different from the in-plane lattice dynamics in AV_3Sb_5 [12]. Furthermore, CDW of ScV_6Sn_6 is easy to tune [21] and exhibits various microscopic features such as critical role of phonons [22–25], large-spin Berry curvature [26], partial band-gap opening [26–28], and hidden magnetism [29]. As the first such member of the versatile kagome family of $HfFe_6Ge_6$-type compounds, it is worthwhile to study the temperature and magnetic field-dependent electrical transport properties of high-quality single crystals of ScV_6Sn_6 in order to obtain information about the Fermi surface (FS) and lattice dynamics, reported in this paper.

ScV_6Sn_6 crystallizes at room temperature in a hexagonal centrosymmetric structure with a $P6/mmm$ space group. The V atoms form a kagome lattice in the ab plane [Fig. 1(a), left], while the Sn atoms sit above and below, separating the lattice [20]. High-quality hexagonal single crystals [Fig. 1(b), inset] were grown by the flux method; see Supplemental Material (SM) [30].

To facilitate further measurements, the crystal orientations were marked in Cartesian coordinates $\hat{x}$, $\hat{y}$, and $\hat{z}$, which correspond to (2 $\bar{1}$ $\bar{1}$ 0), (0 1 $\bar{1}$ 0), and (0 0 0 1) crystallographic directions in the hexagonal crystal structure, respectively. Laue x-ray-diffraction patterns were recorded along $\hat{z}$ and show a clear sixfold symmetry [Fig. 1(a), right]. The patterns fit well with the lattice parameters $a = b = 5.473\,3(5)$ Å and $c = 9.172\,4(8)$ Å derived from the fitting of power x-ray patterns (see Fig. S1 in SM) [30,31]. The measured chemical compositions from the energy-dispersive x-ray spectrum are close to the stoichiometric atomic ratio of Sc : V : Sn = 1 : 5.97 : 6.07. We further cut the crystals in defined orientations of Hall-bar geometry and fabricated four-probe Pt-wire contacts with highly conductive Ag paint. The I-V characteristics at 2 K in different fields are linear [Fig. 1(b)], confirming

*shekhar@cpfs.mpg.de

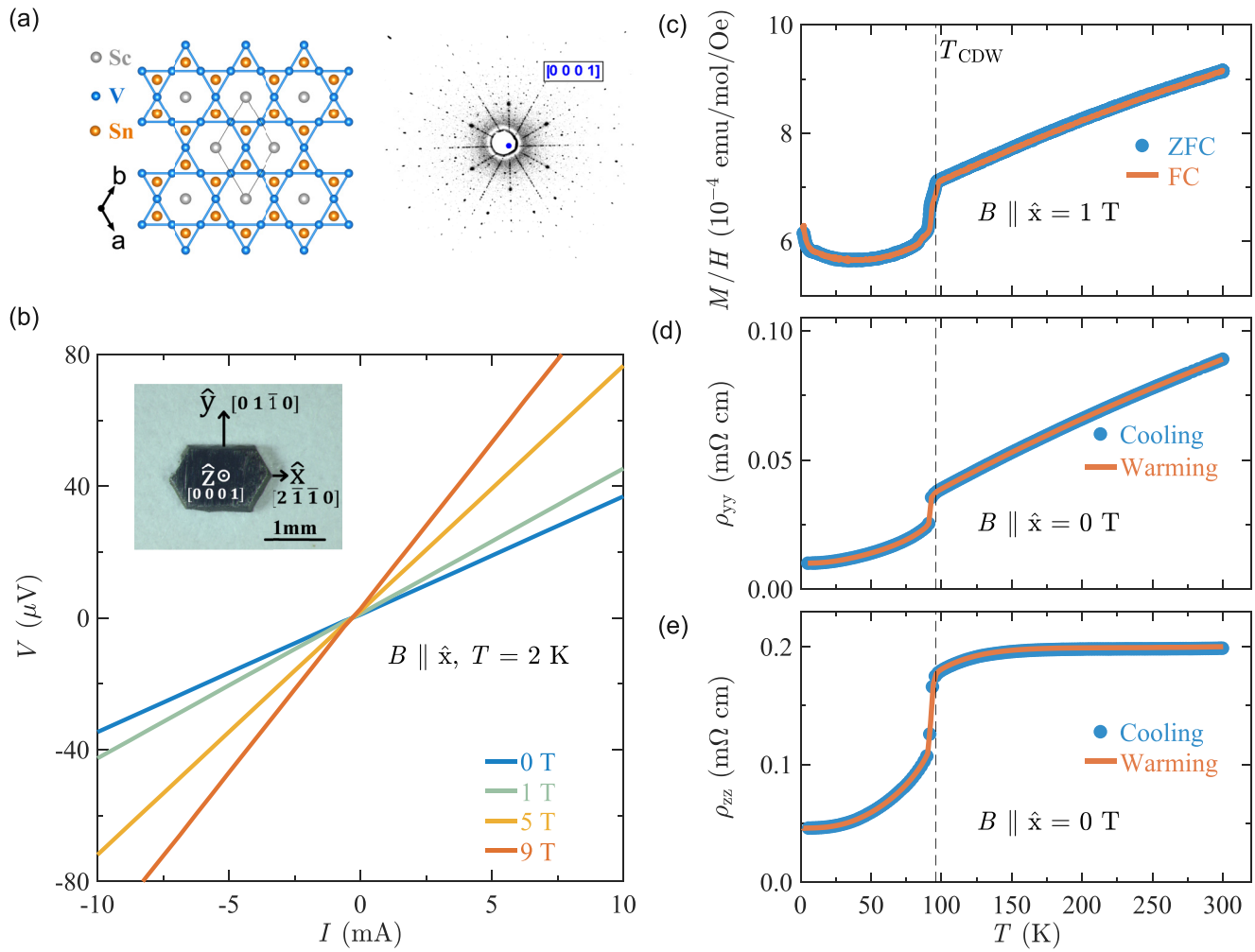

FIG. 1. Kagome lattice, Laue pattern, *I-V* characteristic, and CDW phase transition of ScV_6Sn_6. (a) Kagome lattice of ScV_6Sn_6 viewed along the *c* axis (left) and recorded single-crystal Laue patterns along the *c* axis. (b) *I-V* characteristics at various fields at 2 K. The inset is an optical image of the crystal with Cartesian coordinate. (c) Magnetic susceptibility along $\hat{x}$. Resistivity in zero field (d) along $\hat{y}$ and (c) along $\hat{z}$, where the sudden jumps show CDW phase transition.

the high quality of the ohmic contacts. The appearance of CDW in this compound is a key property, and we found it in the temperature-dependent magnetization and the electrical resistivity [Figs. 1(c)–1(e)]. A sharp transition appears at 92 K, depicting the CDW transition temperature similar to the previous reports [19,20]. The measured magnetic susceptibility in Fig. 1(c) describes a weak Pauli paramagnetic-like behavior, which is different from its structural sister compound YV_6Sn_6 [32]. The zero-field electrical resistivity shows a metallic behavior with temperature, and both ρ_{yy} and ρ_{zz} drop suddenly at the CDW phase transition due to the large softening of the acoustic phonon modes [Figs. 1(d) and 1(e)] [23,24]. The typical values of $\rho_{yy}(\rho_{zz})$ at 2 K are found to be $1 \times 10^{-5}(4.58 \times 10^{-5})\,\Omega$cm and the resulting residual resistivity ratio ($RRR = \rho_{300\,\mathrm{K}}/\rho_{2\,\mathrm{K}}$) is 8.9(4.3). Noticeably, the ρ_{zz} changes significantly from the ρ_{yy} at the CDW phase transition.

After the basic characterization of the crystals, we then focused on the magnetic field, *B*-dependent transverse resistivity, which was measured at different temperatures and angles in the field of ± 9 T. The angular dependence of the field is defined as $\theta(= \hat{x} \rightarrow \hat{z})$ and $\phi(= \hat{x} \rightarrow \hat{y})$, where $0^\circ = B||\hat{x}$, $90^\circ = B||\hat{y}$ or $\hat{z}$. First, we describe the behavior of ρ_{zz} when $B||\hat{x}$ (θ and $\phi = 0$), and the measured data are shown in Fig. S6(a) in SM [30]. At low temperatures, ρ_{zz} exhibits clear Shubnikov–de Haas (SdH) quantum oscillations which are a striking feature that helps to probe the low-energy bands. At 2 K, the quantum oscillation starts from the field around 1.5 T, as seen in Fig. 2(a) for the $d\rho_{zz}/dB$ plot and it is easily visible up to 12 K (see Fig. S6(b) in SM [30]). The magnetoresistance MR ($= \rho_{zz}(B)/\rho_{zz}(0) - 1$) is estimated, and the highest value is found to be 170% at the lowest temperature of 2 K [see Fig. S6(a) in SM) [30]). Unlike the other typical semimetals, e.g., NbP, the present compound ScV_6Sn_6 does not show an extremely large MR [33]. However, the SdH oscillation indicates a low effective mass of the electron charge carrier in the CDW phase [23,24]. To obtain the amplitude of the SdH oscillations, a smooth polynomial background was subtracted from the measured ρ_{zz}. The resultant $\Delta\rho_{zz}$ at several temperatures is plotted as a function of $1/B$, as shown in Fig. 2(b).

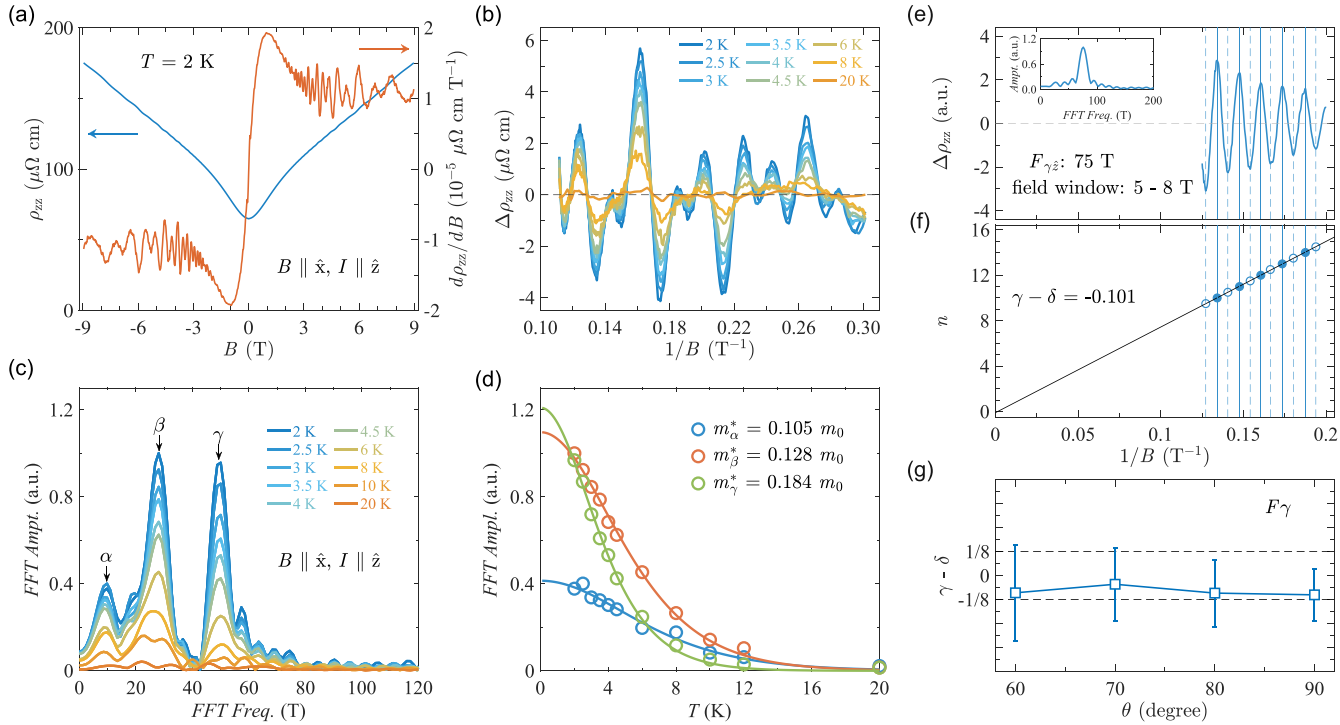

FIG. 2. Shubnikov–de Haas (SdH) oscillations and Berry phase. (a) Longitudinal ρ_{zz} at 2 K and its first derivative with field showing quantum oscillations. (b) Background-subtracted SdH oscillation amplitude at several temperatures. (c) Corresponding FFT amplitude exhibiting α, β, and γ frequencies. (d) FFT amplitude fit estimating effective mass. (e) SdH oscillations when $B||\hat{z}$ and their FFT spectrum (inset) showing only the γ frequency in the field window of 5–8 T. (f) Intercept of the Landau fan diagram revealing nonzero Berry phase. (g) Angular dependence of the Berry phase.

As expected, the oscillations are periodic in $1/B$ and they arise from quantization of the energy level further, forming Landau levels (LLs) [34]. The analysis of the temperature- and field-dependent periodic oscillations provides insight into the fermiology of the compound and the associated physical characteristics of the charge carriers.

In the fast Fourier transform (FFT) of the SdH oscillations presented in Fig. 2(c), we detected the existence of three distinct frequencies: $F_\alpha = 10$ T, $F_\beta = 28$ T, and $F_\gamma = 50$ T. These frequencies indicate the presence of small FSs. Compared to AV_3Sb_5 (A = K, Rb, and Cs), the splitting of FS in ScV_6Sn_6 is simpler. At least nine FSs have been detected in CsV_3Sb_5, with their belonging frequency ranging from 10 to 2000 T [35–38]. Lifshitz-Kosevich (LK) theory is used extensively to analyze the physical properties of FSs [34], and it fully explains the SdH oscillations. The effective mass, Dingle temperature, and phase factor are evaluated using the LK equation, where $\Delta\rho \propto R_T R_D \cos[2\pi(\frac{F}{B} + \gamma - \delta)]$. Specifically, $R_T = 14.69 m^* T/B \times \sinh(14.69 m^* T/B)$ and $R_D = \exp(-14.69 m^* T_D/B)$ are the cyclotron effective mass term and Dingle term, respectively, in which $m^*(m_0)$ is the effective (bare) mass of the electron, B is the average field used in the FFT, and T_D is the Dingle temperature. The phase factor $\gamma - \delta$, which is directly related to the Berry phase within δ, equals to 0 for the 2D system and $\pm\frac{1}{8}$ for the 3D system ($\pm$ corresponds to the contribution from the minimal/maximal cross section) [36,39,40]. Among the various parameters of FSs that can be estimated using the LK formula, the estimation of the Berry phase is very promising for proving the nontrivial topology of the band. Accordingly, we designed the Landau fan diagram by assigning LLs to the oscillatory extrema. The integer nth LLs are assigned to maxima when $\rho_{xx} \gg \rho_{yx}$, while they are assigned to minima when $\rho_{xx} \ll \rho_{yx}$ [36,39,41]. For ScV_6Sn_6 where $\rho_{zz} \sim 10\rho_{yz}$, which satisfies the condition of $\rho_{xx} \gg \rho_{yx}$, the integer nth are assigned to the maxima and the half-integer $(n + \frac{1}{2})$th are assigned minimum of $\Delta\rho_{zz}$, as shown in Figs. 2(e) and 2(f). The Landau indices n and $1/B$ satisfy the Lifshitz-Onsager relationship, which is described by the equation $n = \frac{F}{B} + \gamma - \delta$. The slope of the plot between n and $1/B$ provides the oscillatory frequency, while the intercept offers the information on the Berry phase. To attain an accurate estimation of the Berry phase of F_γ, we selected a field window between 5 and 8 T to exclude the weak F_α oscillatory component [Fig. 2(e), inset]. From Fig. 2(f), the intercept of the Landau fan diagram for F_γ in terms of the phase factor $\gamma - \delta$ is estimated to be -0.101, indicating a nontrivial Berry phase [42,43]. Similarly, we obtained the Berry phase further for the angular dependence of the field from $\hat{x}$ to $\hat{z}$ without interference from the other exiting frequencies, and the values are given in Fig. 2(g). The figure indicates the Berry phase factor $\gamma - \delta$ falls within the range of $0 \pm \frac{1}{8}$ for $\theta \geqslant 60°$. While it is possible to estimate the Berry phase factor $\theta > 20°$, since the F_β is absent, but the SdH amplitude declines rapidly. At all other angles of θ and ϕ, the F_β is consistently present [see in Fig. 4(b)], which intervenes the amplitude in terms of the beating patterns [44,45], as can be seen in Figs. S9(c)

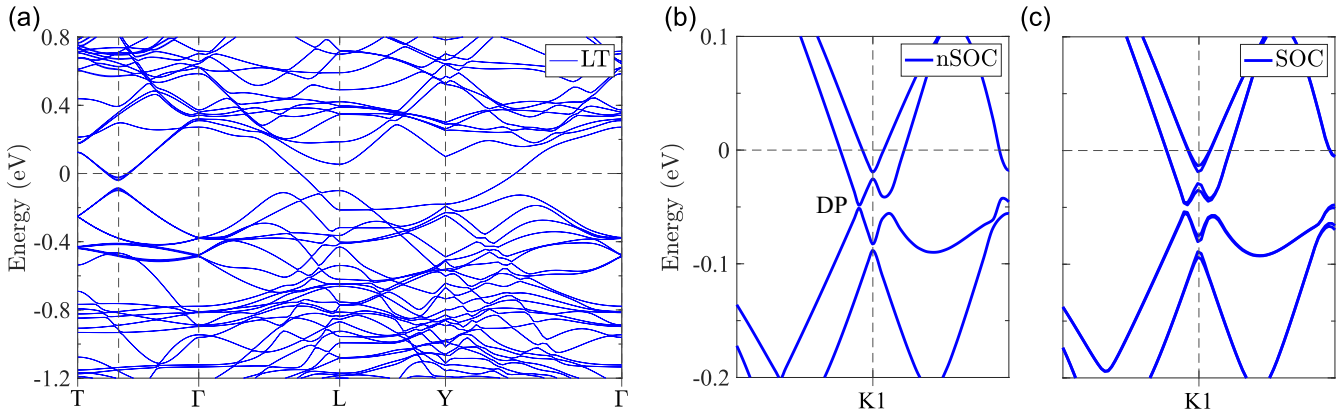

FIG. 3. Band structure in charge-density wave (CDW) phase. (a) Band structure of ScV_6Sn_6 CDW phase with the presence of spin-orbital coupling (SOC). The structural parameters are the same as in Ref. [20] at 50 K. The magnified view of the band structure around $K1$ locating the Dirac point (DP) (b) without the SOC and (c) with the SOC.

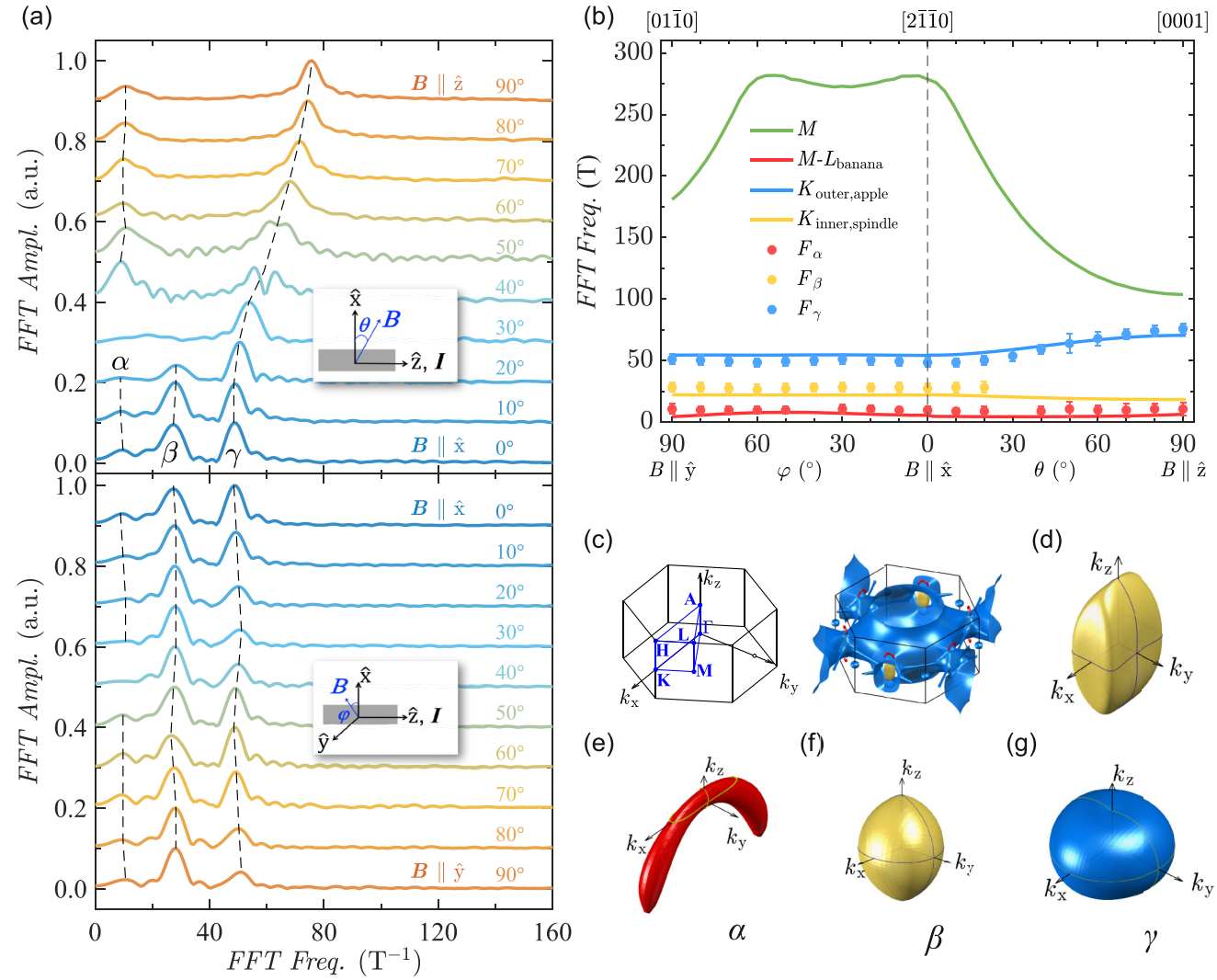

FIG. 4. SdH oscillations and fermiology. (a) SdH oscillation frequency at different rotating angles $\theta(=\hat{x}\rightarrow\hat{z})$ and $\phi(=\hat{x}\rightarrow\hat{y})$, where dotted lines represent their tracking with angle. The insets show a sketch of the field rotation. (b) Angular dependence of $F_{\alpha,\beta,\gamma}$, where $F_{\alpha,\beta}$ do not change while F_γ shifts slightly. Solid lines are corresponding calculated frequencies. The error bar is taken from the half-width of the half maximum value of the frequency peaks. (c) Brillouin zone and three-dimensional (3D) Fermi surfaces (FSs) at the Fermi energy. (d)–(g) Enlarged FSs, including the FS at M point (d, yellow), the banana-shaped α pocket along M-L (e, red), the spindle-shaped inner β pocket at K point (f, yellow), and the apple-shaped outer γ pocket at K point (g, blue).

and S9(d) in SM [30]. One method to separate the amplitude corresponding to each frequency is to use the bandpassing filter as shown in Figs. S6(c) and S6(d) in SM) [30,46], but may not be very reliable. We also tried to estimate the Berry phase related to F_α and F_β. As we can see, F_α shows very weak oscillatory amplitude with limited cycle up to 9 T. One the other hand, the presence of the beating patterns harms the amplitude of the F_β, which only appears for $\theta \leqslant 20^\circ$, and after that the F_β vanishes. These together make it difficult to carry out the Berry phase analysis for F_α and F_β.

To determine the effective mass for the carriers corresponding to each FS, the temperature dependence of the amplitude of each peak in the FFT is plotted, and then it is fitted with an R_T term [Fig. 2(d)] from the LK formula. From these fittings, we find the values of $m^*_{\alpha,\beta,\gamma} = 0.105\, m_0$, $0.128\, m_0$, and $0.184\, m_0$. These masses are very low (even lower than CsV_3Sb_5 [35,36]). Furthermore, the Dingle temperature T_D can be estimated from the semilog plot described by $\ln(A/R_T) \propto -14.69 m^* T_D/B$ (see Fig. S8 in SM) [30], where A corresponds to the amplitude of the SdH oscillations. We found T_D to be 2.5 K for γ pocket and the corresponding quantum scattering time τ_q is $\sim 5 \times 10^{-13}$ s. For the $F_{\alpha,\beta,\gamma} = 10$, 28, and 50 T, the equivalent periodicities $1/(F_{\alpha,\beta,\gamma}) = 0.1$, 0.036, and $0.02\,T^{-1}$, which are further related to the cross-sectional area A_F of FS by the Onsager relation $F = (\Phi_0/2\pi^2)A_F$, where the value of magnetic flux quantum $\Phi_0 = 2.068 \times 10^{-15}$ Wb. The corresponding area $A_{F\alpha,\beta,\gamma} = 0.001$, 0.0027, and 0.0048 $Å^{-2}$. Assuming a circular cross section of these FSs for simplicity, the very small Fermi vectors $k_{F\alpha,\beta,\gamma} = 0.017$, 0.029, and 0.039 $Å^{-1}$ are found, and their corresponding Fermi velocities $v_{F\alpha,\beta,\gamma}$ are 1.92×10^5, 2.64×10^5, and $2.45 \times 10^5 m\,s^{-1}$. Additional relevant experimental parameters of the FSs are summarized in Table S1 in SM [30].

To capture the topology in electronic band structure of ScV_6Sn_6, we performed detailed band-structure calculations by using density-functional theory (DFT). Due to the presence of CDW transition, we transformed the band structure of low-temperature (LT) phase into the high-temperature (HT) phase, the LT phase (CDW phase) has been characterized at a temperature of 50 K, and the lattice parameters are taken from the previous report [20]. From Fig. S11 in SM [30], the unfolded band structures of LT and HT phases are in a good agreement with the angle-resolved photoemission spectrum experiment [27]. Among the two phases, the major change in the electronic band structure appears only along the *A-L-H* direction (where the band opens a gap because of the CDW transition [27]), while the van Hove singularity bands at the *M* point and the Dirac bands at the *K* point do not change. From a closer view, a fascinating feature depicted in Fig. 3(a) is the band-folding phenomenon, whereby the original *K* point at coordinates (1/3, 1/3, 0) transmutes into a folded *K*1 point situated at (1/3, 1/3, −2/3). This figure unambiguously reveals that the *K*1 point intrinsically possesses a substantial band gap near the Fermi energy (E_F). Furthermore, both the conduction- and valence bands are completely split at this point, implying the absence of topologically protected Dirac points. Utilizing the transformation matrix, we ascertain that the original *M* point at (1/2, 0, 0) and the Γ point at (0, 0, 0) have been mapped to the *M*1 point at (1/2, 0, −1/2) and Γ point at (0, 0, 0), respectively. As a result, we discovered that the genuine Dirac point [labeled as DP in Fig. 3(b)] has been mapped to the position of (0.341666, 0.316 666, −0.658327). From this magnified view of the band structure near this point, its Dirac nature is clearly confirmed. Similar to the Dirac points in graphene systems, this point develops a band gap when considering spin-orbit coupling as shown in Fig. 3(c), and gives rise to nontrivial topological properties. Therefore, we believe that the nontrivial π Berry phase extracted in the SdH oscillation actually comes from the electron pockets formed in the energy bands where the DP is located.

To gain more information about the topography of the FS, we measured the angular $\theta(=\hat{x} \to \hat{z})$ and $\phi(=\hat{x} \to \hat{y})$-dependent oscillations. The rotating angles of field with the crystal axes are sketched in the insets of Fig. 4(a), where $0^\circ = B||\hat{x}$ and $90^\circ = B||\hat{y}$ or $\hat{z}$. The angular-dependent FFT is plotted in Fig. 4(a). As we mentioned earlier, the three frequencies, namely α, β, and γ, appear when $B\|\hat{x}$. Depending upon the shape of FS, the movement of frequency depends on the rotating angle. From Fig. 4(a), we carefully tracked the position of all visible frequencies with the rotating angles as demonstrated in Fig. 4(b). This indicates that when the field B moves either from the $\hat{x} \to \hat{y}$ or $\hat{x} \to \hat{z}$, the frequencies α, β and γ change slightly. Noticeably, when the $\theta > 20^\circ$, the β disappears. This helps further to improve the accuracy of Berry phase analysis related to γ. In order to allocate the experimentally observed frequencies, we theoretically calculated 3D FSs and their corresponding frequency from the unfolded band structure of the LT phase. As we can see in Fig. 4(b), all observed frequencies are accurately replicated by the calculated 3D FSs, except for higher frequency (green line). In addition, the calculated F_β is present at all angles, but it disappears at $\theta > 20^\circ$ in the experiment, which needs further investigation. Figure 4(c) shows 3D FSs within the Brillouin zone (BZ), in which a large electron pocket (blue color) around Γ covers the whole BZ, together with a small banana-shaped FS (red color) along the *M-L* direction, a small apple-shaped FS (blue color) at *K*, and a larger FS at *M* (yellow color). There is another spindle-shaped FS at *K*, which comes from the same band with the FS at *M* and is covered by the apple-shaped pocket. After comparing with DFT results, we found that the F_α belongs to the banana-shaped FS [Fig. 4(e)]. The F_β belongs to the spindle-shaped FS [Fig. (4f)]. The F_γ is part of the apple-shaped FS that is contributed by the Dirac bands [Fig. 4(g)], exhibiting the nontrivial Berry phase. The calculated high frequency [green solid line in Fig. 4(b)] comes from the FS [Fig. 4(d)] at the *M* point, which is not detectable up to 9 T in the present measurements.

After exploring the striking features of the FS, we now get the insight of classical Drude transport from the Hall resistivity ρ_{zy} for current $I||\hat{y}$ and $B||\hat{x}$. From these data, the Hall constant $R_H(=\rho_{zy}/B)$ was calculated by considering the high field slope between 6 and 9 T at different temperatures [Fig. 5(a), inset], resulting in electron density $n(=1/eR_H)$ and mobility $\mu(=R_H/\rho_{yy})$ of 2.4×10^{21} cm^{-3} and $265\,cm^2V^{-1}s^{-1}$ at 2 K, respectively (see Fig. S3(c) in

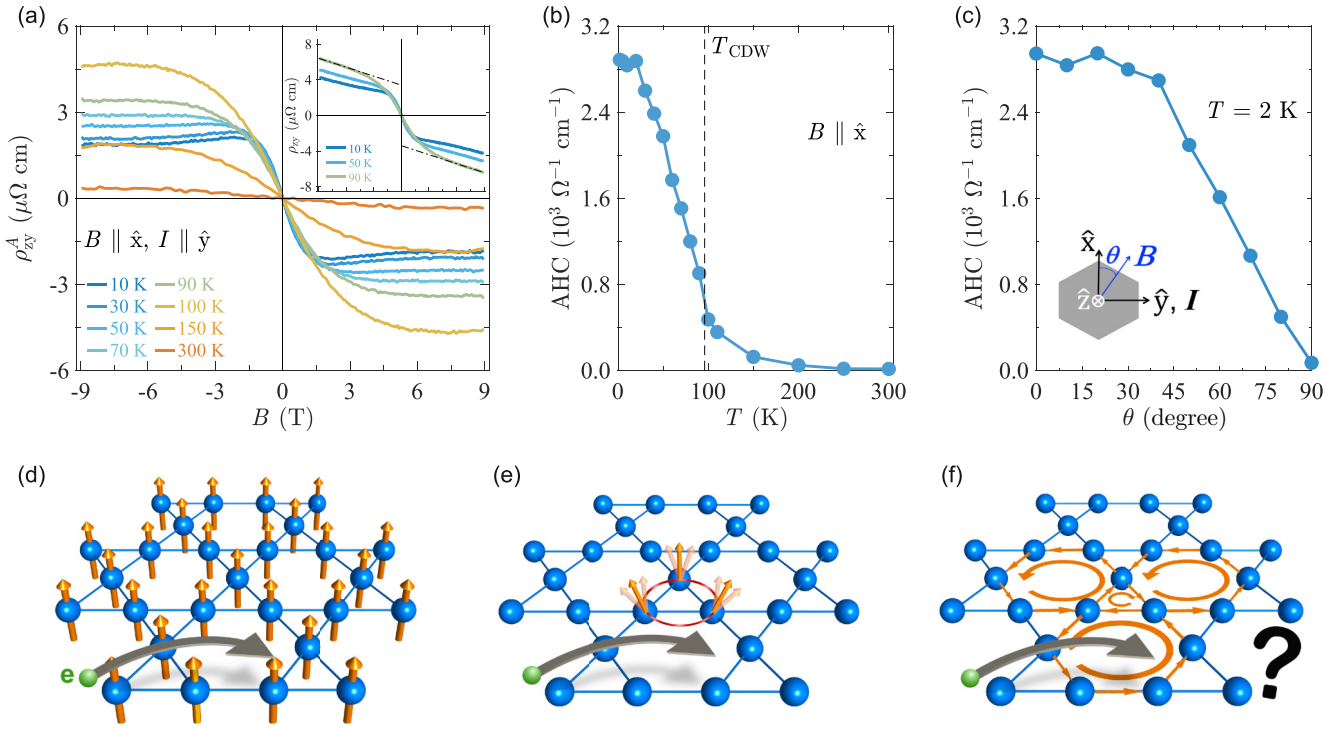

FIG. 5. Anomalous Hall-like behavior in ScV_6Sn_6. (a) Field-dependent measured anomalous behavior of Hall resistivity, ρ_{zy} at various temperatures (inset) and extracted Hall resistivity ρ_{zy}^A. (b) Temperature and (c) angular-dependent corresponding anomalous Hall-like conductivity. Electrons picking up anomalous velocity from the different sources and their typical example. (d) Nonzero Berry phase from ferromagnetic spins. (e) Topological orbital moment due to spin chirality. (f) Formation of local loop currents.

SM [30]). The Drude scattering time, $\tau_{tr} = \mu m^*/e = 2.1 \times 10^{-14}$s, where m^* is $0.139m_0$ (the average of m^*) and e is the elementary charge. The ratio of $\tau_c/\tau_{tr}(\sim 25)$ is large, where τ_c and τ_{tr} are related to electron-electron and electron-phonon scattering processes, respectively. Besides the usual high- and low-angle scattering mechanisms, the large lowering value of τ_{tr} could be related to the phonon modes, arising from promoting the electron-phonon coupling crucially in the CDW phase [22–24].

The field-dependent ρ_{zy} shows a nonlinear behavior, which is primarily thought to be the presence of multicarriers in a nonmagnetic system such as ScV_6Sn_6, since the multiple bands are around the E_F. To clarify this apparent reason, we fitted both the Hall and longitudinal conductivities by using the standard two-band model (see Fig. S5 in SM) [30,47–50]. Both fits are seemingly good, but their fitted parameters are very different from each other. The fitting of the σ_{yz} reflects both electron carriers, while the fitting of σ_{yy} shows both electron and hole carriers. For the implementation of a reliable and accurate model, the parameters from both fittings must be the same within the error bar as reported in the typical multiband systems [49,50]. Therefore, given the type of carriers, the concentrations and mobilities are highly inconsistent, indicating that the two-band model may not be applicable to the nonlinear Hall effect for ScV_6Sn_6. It is also worthy to note here that the Hall resistivity from a typical multiband system is nonlinear close to zero field, while it becomes linear at high field [33,51–53]. In contrast, the present compound ScV_6Sn_6 shows the linear Hall close to zero field and it bends at high field (>2 T) like a typical soft ferromagnetic system [54,55]. By considering the anomalous behavior naively, we subtracted the linear part from the high field and the anomalous part of the Hall resistivity at different temperatures as shown in Fig. 5(a). Like in soft ferromagnet, an anomaly in the ρ_{zy} (a sharp increase at a lower field followed by saturation with a further increase in the field) is observed, which is attributed to anomalous Hall-like behavior. Such an anomaly usually appears as a hallmark in magnetic systems and it resembles the magnetization curve, wherein magnetic spins play the role [Figs. 5(d) and 5(e)]. However, magnetization is linear with the field (see Fig. S2 in SM) [30] and does not follow the Hall resistivity in the present case. The as-calculated value of anomalous Hall conductivity (AHC $\approx \frac{\rho_{zy}^A}{\rho_{zz}\rho_{yy}}$ since $\rho_{yy} \neq \rho_{zz}$) at 2 K is $3.2 \times 10^3\ \Omega^{-1}\,\text{cm}^{-1}$, which is smaller than AV_3Sb_5 systems [14,15,38]. The AHC remains almost constant up to 45° and starts to decrease with increasing angle further [Fig. 5(c)], while it sustains up to the CDW transition temperature. In contrast to the involvement of magnetism [Figs. 5(d) and 5(e)], one of the possible explanations could be similar to the origin in AV_3Sb_5 [Fig. 5(f)], where the CDW forms a current loop and breaks the time-reversal symmetry (TRS) [16,56,57], since ScV_6Sn_6 also breaks the TRS measured by the muon spectroscopy [29] and to speculate such loop current is a bit premature. In the present scenario, it is difficult to understand the observed Hall behavior of ScV_6Sn_6,

and needs further study. Moreover, the behavior of ρ_{yz} is closer to $ZrTe_5$, assuming the presence of a single Dirac band that splits into a pair of Weyl points in the presence of the magnetic field [58]. However, several bands are present in ScV_6Sn_6, where the concept of Weyl points is not easily applicable.

In conclusion, with the help of field-dependent electrical transports and theoretical calculations, we have revealed the fermiology of ScV_6Sn_6. Along with a large FS, the BZ comprises the several other small-electron FSs, except for the one tiny hole FS. The small FSs exhibit SdH oscillations, resulting in the small effective mass, and the symmetric and asymmetric nature of the FSs for electron and hole, respectively. The electron Dirac band located at the K point gives rise to the nonzero Berry phase, proving that it is a nontrivial topological FS. Furthermore, the nonlinear Hall, which resembles the anomalous Hall, does not fit well with the two-carrier model. Finding the microscopic origins for the anomalous Hall-like signal remains an important issue that requires further theoretical and experimental investigations.

Note added. During the preparation of our work, a similar work including anomalous Hall-like behavior in ScV_6Sn_6 was found [59].

ACKNOWLEDGMENTS

This work was financially supported by the Deutsche Forschungsgemeinschaft (DFG) under SFB1143 (Project No. 247310070), the Würzburg-Dresden Cluster of Excellence on Complexity and Topology in Quantum Matter—ct.qmat (EXC 2147, Project No. 390858490), and Grant No. QUAST-FOR5249-449872909. S.R. thanks the Alexander von Humboldt Foundation for a fellowship. Y.Z. is supported by the startup fund at University of Tennessee Knoxville.

APPENDIX A: MAGNETIC AND ELECTRICAL MEASUREMENTS

Temperature-dependent susceptibility (2–300 K) under various magnetic fields was measured in zero-field-cooled and field-cooled configuration in a Magnetic Properties Measurement System (MPMS, Quantum Design Inc.) equipped with a Superconducting Quantum Interference Device - Vibrating Sample Magnetometer (SQUID-VSM) option. Temperature-dependent four-probe transverse and Hall resistivities were measured on a standard rotating sample holder in a Physical Property Measurement System (PPMS, Quantum Design Inc.). The alternative current transport option was used for measurement with an excitation current of 1.5 mA at a fixed frequency of 93 Hz. Data were collected in the temperature range of 2–300 K, and the magnetic field range of −9 to 9 T in sweep mode.

APPENDIX B: ELECTRONIC BAND-STRUCTURE CALCULATIONS

Ab initio calculations were performed using DFT implemented in the Vienna *Ab initio* Simulation Package (VASP) [60,61]. The projector augmented-wave method [62] and the generalized gradient approximation with Perdew-Burke-Ernzerhof exchange-correlation functional [63] were used for the calculation. Here, we used refined lattice parameters for the band-structure calculations, including the pristine structure and the CDW structure. A $15 \times 15 \times 7\,k$ mesh was used to sample the Brillouin zone of the pristine structure, with an energy cutoff of 500 eV. For the CDW structure, an $8 \times 8 \times 8\,k$ mesh was used, with an energy cutoff of 450 eV. The CDW band structures were unfolded using the VASPKIT toolkit [64]. To obtain the quantum oscillation frequencies, we constructed a Wannier tight-binding Hamiltonian using the WANNIER90 code [65], including Sc $3d$, V $3d$, and Sn $5p$ orbitals.

[1] L.-K. Lim, J.-N. Fuchs, F. Piéchon, and G. Montambaux, Dirac points emerging from flat bands in Lieb-kagome lattices, Phys. Rev. B **101**, 045131 (2020).

[2] M. Li, Q. Wang, G. Wang, Z. Yuan, W. Song, R. Lou, Z. Liu, Y. Huang, Z. Liu, H. Lei *et al.*, Dirac cone, flat band and saddle point in kagome magnet YMn_6Sn_6, Nat. Commun. **12**, 3129 (2021).

[3] W.-S. Wang, Z.-Z. Li, Y.-Y. Xiang, and Q.-H. Wang, Competing electronic orders on kagome lattices at van Hove filling, Phys. Rev. B **87**, 115135 (2013).

[4] Y. Hu, X. Wu, Y. Yang, S. Gao, N. C. Plumb, A. P. Schnyder, W. Xie, J. Ma, and M. Shi, Tunable topological Dirac surface states and van Hove singularities in kagome metal GdV_6Sn_6, Sci. Adv. **8**, eadd2024 (2022).

[5] B. R. Ortiz, S. M. L. Teicher, Y. Hu, J. L. Zuo, P. M. Sarte, E. C. Schueller, A. M. M. Abeykoon, M. J. Krogstad, S. Rosenkranz, R. Osborn *et al.*, CsV_3Sb_5: A Z_2 topological kagome metal with a superconducting ground state, Phys. Rev. Lett. **125**, 247002 (2020).

[6] H.-M. Guo and M. Franz, Topological insulator on the kagome lattice, Phys. Rev. B **80**, 113102 (2009).

[7] B. R. Ortiz, L. C. Gomes, J. R. Morey, M. Winiarski, M. Bordelon, J. S. Mangum, I. W. H. Oswald, J. A. Rodriguez-Rivera, J. R. Neilson, S. D. Wilson *et al.*, New kagome prototype materials: Discovery of KV_3Sb_5, RbV_3Sb_5, and CsV_3Sb_5, Phys. Rev. Mater. **3**, 094407 (2019).

[8] J.-X. Yin, W. Ma, T. A. Cochran, X. Xu, S. S. Zhang, H.-J. Tien, N. Shumiya, G. Cheng, K. Jiang, B. Lian *et al.*, Quantum-limit Chern topological magnetism in $TbMn_6Sn_6$, Nature (London) **583**, 533 (2020).

[9] L. Zheng, Z. Wu, Y. Yang, L. Nie, M. Shan, K. Sun, D. Song, F. Yu, J. Li, D. Zhao *et al.*, Emergent charge order in pressurized kagome superconductor CsV_3Sb_5, Nature (London) **611**, 682 (2022).

[10] X. Wu, T. Schwemmer, T. Müller, A. Consiglio, G. Sangiovanni, D. Di Sante, Y. Iqbal, W. Hanke, A. P. Schnyder, M. M. Denner *et al.*, Nature of unconventional pairing in the

kagome superconductors AV_3Sb_5(A = K, Rb, Cs), Phys. Rev. Lett. **127**, 177001 (2021).

[11] X. Teng, L. Chen, F. Ye, E. Rosenberg, Z. Liu, J.-X. Yin, Y.-X. Jiang, J. S. Oh, M. Z. Hasan, K. J. Neubauer *et al.*, Discovery of charge density wave in a kagome lattice antiferromagnet, Nature (London) **609**, 490 (2022).

[12] H. Tan, Y. Liu, Z. Wang, and B. Yan, Charge density waves and electronic properties of superconducting kagome metals, Phys. Rev. Lett. **127**, 046401 (2021).

[13] X. Feng, K. Jiang, Z. Wang, and J. Hu, Chiral flux phase in the kagome superconductor AV_3Sb_5, Sci. Bull. **66**, 1384 (2021).

[14] F. H. Yu, T. Wu, Z. Y. Wang, B. Lei, W. Z. Zhuo, J. J. Ying, and X. H. Chen, Concurrence of anomalous Hall effect and charge density wave in a superconducting topological kagome metal, Phys. Rev. B **104**, L041103 (2021).

[15] S.-Y. Yang, Y. Wang, B. R. Ortiz, D. Liu, J. Gayles, E. Derunova, R. Gonzalez-Hernandez, L. Šmejkal, Y. Chen, S. S. P. Parkin *et al.*, Giant, unconventional anomalous Hall effect in the metallic frustrated magnet candidate, KV_3Sb_5, Sci. Adv. **6**, eabb6003 (2020).

[16] C. Mielke, D. Das, J.-X. Yin, H. Liu, R. Gupta, Y.-X. Jiang, M. Medarde, X. Wu, H. C. Lei, J. Chang *et al.*, Time-reversal symmetry-breaking charge order in a kagome superconductor, Nature (London) **602**, 245 (2022).

[17] H. Li, H. Zhao, B. R. Ortiz, T. Park, M. Ye, L. Balents, Z. Wang, S. D. Wilson, and I. Zeljkovic, Rotation symmetry breaking in the normal state of a kagome superconductor KV_3Sb_5, Nat. Phys. **18**, 265 (2022).

[18] C. Guo, C. Putzke, S. Konyzheva, X. Huang, M. Gutierrez-Amigo, I. Errea, D. Chen, M. G. Vergniory, C. Felser, M. H. Fischer *et al.*, Switchable chiral transport in charge-ordered kagome metal CsV_3Sb_5, Nature (London) **611**, 461 (2022).

[19] X. Teng, J. S. Oh, H. Tan, L. Chen, J. Huang, B. Gao, J.-X. Yin, J.-H. Chu, M. Hashimoto, D. Lu *et al.*, Magnetism and charge density wave order in kagome FeGe, Nat. Phys. **19**, 814 (2023).

[20] H. W. S. Arachchige, W. R. Meier, M. Marshall, T. Matsuoka, R. Xue, M. A. McGuire, R. P. Hermann, H. Cao, and D. Mandrus, Charge density wave in kagome lattice intermetallic ScV_6Sn_6, Phys. Rev. Lett. **129**, 216402 (2022).

[21] X. Zhang, J. Hou, W. Xia, Z. Xu, P. Yang, A. Wang, Z. Liu, J. Shen, H. Zhang, X. Dong *et al.*, Destabilization of the charge density wave and the absence of superconductivity in ScV_6Sn_6 under high pressures up to 11 GPa, Materials **15**, 7372 (2022).

[22] Y. Hu, J. Ma, Y. Li, D. J. Gawryluk, T. Hu, J. Teyssier, V. Multian, Z. Yin, Y. Jiang, S. Xu *et al.*, Phonon promoted charge density wave in topological kagome metal ScV_6Sn_6, arXiv:2304.06431.

[23] T. Hu, H. Pi, S. Xu, L. Yue, Q. Wu, Q. Liu, S. Zhang, R. Li, X. Zhou, J. Yuan *et al.*, Optical spectroscopy and band structure calculations of the structural phase transition in the vanadium-based kagome metal ScV_6Sn_6, Phys. Rev. B **107**, 165119 (2023).

[24] A. Korshunov, H. Hu, D. Subires, Y. Jiang, D. Călugăru, X. Feng, A. Rajapitamahuni, C. Yi, S. Roychowdhury, M. G. Vergniory *et al.*, Softening of a flat phonon mode in the kagome ScV_6Sn_6, Nat. Commun. **14**, 6646 (2023).

[25] Y. Gu, E. T. Ritz, W. R. Meier, A. Blockmon, K. Smith, R. P. Madhogaria, S. Mozaffari, D. Mandrus, T. Birol, and J. L. Musfeldt, Phonon mixing in the charge density wave state of ScV_6Sn_6, npj Quantum Mater. **8**, 58 (2023).

[26] D. Di Sante, C. Bigi, P. Eck, S. Enzner, A. Consiglio, G. Pokharel, P. Carrara, P. Orgiani, V. Polewczyk, J. Fujii *et al.*, Flat band separation and robust spin Berry curvature in bilayer kagome metals, Nat. Phys. **19**, 1135 (2023).

[27] S. Cheng, Z. Ren, H. Li, J. Oh, H. Tan, G. Pokharel, J. M. DeStefano, E. Rosenberg, Y. Guo, Y. Zhang *et al.*, Nanoscale visualization and spectral fingerprints of the charge order in ScV_6Sn_6 distinct from other kagome metals, arXiv:2302.12227.

[28] S. Lee, C. Won, J. Kim, J. Yoo, S. Park, J. Denlinger, C. Jozwiak, A. Bostwick, E. Rotenberg, R. Comin *et al.*, Nature of charge density wave in kagome metal ScV_6Sn_6, arXiv:2304.11820.

[29] Z. Guguchia, D. J. Gawryluk, S. Shin, Z. Hao, C. Mielke, III, D. Das, I. Plokhikh, L. Liborio, K. Shenton, Y. Hu *et al.*, Hidden magnetism uncovered in charge ordered bilayer kagome material ScV_6Sn_6, Nat. Commun. **14**, 7796 (2023).

[30] See Supplemental Material at http://link.aps.org/supplemental/10.1103/PhysRevB.109.035124 for growth method, structural and chemical component characterization of single-crystal ScV_6Sn_6; magnetic properties; additional electromagnetic transport properties; and calculated electronic band structures.

[31] J. Rodríguez-Carvajal, Recent advances in magnetic structure determination by neutron powder diffraction, Physica B **192**, 55 (1993).

[32] G. Pokharel, S. M. L. Teicher, B. R. Ortiz, P. M. Sarte, G. Wu, S. Peng, J. He, R. Seshadri, and S. D. Wilson, Electronic properties of the topological kagome metals YV_6Sn_6 and GdV_6Sn_6, Phys. Rev. B **104**, 235139 (2021).

[33] C. Shekhar, A. K. Nayak, Y. Sun, M. Schmidt, M. Nicklas, I. Leermakers, U. Zeitler, Y. Skourski, J. Wosnitza, Z. Liu *et al.*, Extremely large magnetoresistance and ultrahigh mobility in the topological weyl semimetal candidate NbP, Nat. Phys. **11**, 645 (2015).

[34] D. Shoenberg, *Magnetic Oscillations in Metals* (Cambridge University Press, Cambridge, 1984).

[35] B. R. Ortiz, S. M. L. Teicher, L. Kautzsch, P. M. Sarte, N. Ratcliff, J. Harter, J. P. C. Ruff, R. Seshadri, and S. D. Wilson, Fermi surface mapping and the nature of charge-density-wave order in the kagome superconductor CsV_3Sb_5, Phys. Rev. X **11**, 041030 (2021).

[36] Y. Fu, N. Zhao, Z. Chen, Q. Yin, Z. Tu, C. Gong, C. Xi, X. Zhu, Y. Sun, K. Liu *et al.*, Quantum transport evidence of topological band structures of kagome superconductor CsV_3Sb_5, Phys. Rev. Lett. **127**, 207002 (2021).

[37] K. Shrestha, M. Shi, B. Regmi, T. Nguyen, D. Miertschin, K. Fan, L. Z. Deng, N. Aryal, S.-G. Kim, D. E. Graf *et al.*, High quantum oscillation frequencies and nontrivial topology in kagome superconductor KV_3Sb_5 probed by torque magnetometry up to 45 T, Phys. Rev. B **107**, 155128 (2023).

[38] Y. Wang, Z. Chen, Y. Nie, Y. Zhang, Q. Niu, G. Zheng, X. Zhu, W. Ning, and M. Tian, Nontrivial fermi surface topology and large anomalous Hall effect in the kagome superconductor RbV_3Sb_5 Phys. Rev. B **108**, 035117 (2023).

[39] Y. Ando, Topological insulator materials, J. Phys. Soc. Jpn. **82**, 102001 (2013).

[40] A. A. Taskin, S. Sasaki, K. Segawa, and Y. Ando, Manifestation of topological protection in transport properties of epitaxial Bi_2Se_3 thin films, Phys. Rev. Lett. **109**, 066803 (2012).

[41] F.-X. Xiang, X.-L. Wang, M. Veldhorst, S.-X. Dou, and M. S. Fuhrer, Observation of topological transition of Fermi surface from a spindle torus to a torus in bulk Rashba spin-split BiTeCl, Phys. Rev. B **92**, 035123 (2015).

[42] H. Murakawa, M. S. Bahramy, M. Tokunaga, Y. Kohama, C. Bell, Y. Kaneko, N. Nagaosa, H. Y. Hwang, and Y. Tokura, Detection of Berry's phase in a bulk Rashba semiconductor, Science **342**, 1490 (2013).

[43] D.-X. Qu, Y. S. Hor, J. Xiong, R. J. Cava, and N. P. Ong, Quantum oscillations and Hall anomaly of surface states in the topological insulator Bi_2Te_3, Science **329**, 821 (2010).

[44] X. Xu, X. Wang, T. A. Cochran, D. S. Sanchez, G. Chang, I. Belopolski, G. Wang, Y. Liu, H.-J. Tien, X. Gui *et al.*, Crystal growth and quantum oscillations in the topological chiral semimetal CoSi, Phys. Rev. B **100**, 045104 (2019).

[45] N. Huber, K. Alpin, G. L. Causer, L. Worch, A. Bauer, G. Benka, M. M. Hirschmann, A. P. Schnyder, C. Pfleiderer, and M. A. Wilde, Network of topological nodal planes, multifold degeneracies, and weyl points in CoSi, Phys. Rev. Lett. **129**, 026401 (2022).

[46] M. N. Ali, L. M. Schoop, C. Garg, J. M. Lippmann, E. Lara, B. Lotsch, and S. S. P. Parkin, Butterfly magnetoresistance, quasi-2D Dirac Fermi surface and topological phase transition in ZrSiS, Sci. Adv. **2**, e1601742 (2016).

[47] N. Bansal, Y. S. Kim, M. Brahlek, E. Edrey, and S. Oh, Thickness-independent transport channels in topological insulator Bi_2Se_3 thin films, Phys. Rev. Lett. **109**, 116804 (2012).

[48] F. C. Chen, Y. Fei, S. J. Li, Q. Wang, X. Luo, J. Yan, W. J. Lu, P. Tong, W. H. Song, X. B. Zhu *et al.*, Temperature-induced lifshitz transition and possible excitonic instability in ZrSiSe, Phys. Rev. Lett. **124**, 236601 (2020).

[49] J. Xu, Y. Wang, S. E. Pate, Y. Zhu, Z. Mao, X. Zhang, X. Zhou, U. Welp, W.-K. Kwok, D. Y. Chung *et al.*, Unreliability of two-band model analysis of magnetoresistivities in unveiling temperature-driven Lifshitz transition, Phys. Rev. B **107**, 035104 (2023).

[50] Y. L. Wang, L. R. Thoutam, Z. L. Xiao, J. Hu, S. Das, Z. Q. Mao, J. Wei, R. Divan, A. Luican-Mayer, G. W. Crabtree *et al.*, Origin of the turn-on temperature behavior in WTe_2, Phys. Rev. B **92**, 180402 (2015).

[51] X. Huang, L. Zhao, Y. Long, P. Wang, D. Chen, Z. Yang, H. Liang, M. Xue, H. Weng, Z. Fang *et al.*, Observation of the chiral-anomaly-induced negative magnetoresistance in 3D weyl semimetal TaAs, Phys. Rev. X **5**, 031023 (2015).

[52] N. Kumar, Y. Sun, N. Xu, K. Manna, M. Yao, V. Süss, I. Leermakers, O. Young, T. Förster, M. Schmidt *et al.*, Extremely high magnetoresistance and conductivity in the type-II weyl semimetals WP_2 and MoP_2, Nat. Commun. **8**, 1642 (2017).

[53] J. A. Voerman, L. Mulder, J. C. De Boer, Y. Huang, L. M. Schoop, C. Li, and A. Brinkman, Origin of the butterfly magnetoresistance in ZrSiS, Phys. Rev. Mater. **3**, 084203 (2019).

[54] K. Manna, L. Muechler, T.-H. Kao, R. Stinshoff, Y. Zhang, J. Gooth, N. Kumar, G. Kreiner, K. Koepernik, R. Car *et al.*, From colossal to zero: Controlling the anomalous Hall effect in magnetic Heusler compounds via Berry curvature design, Phys. Rev. X **8**, 041045 (2018).

[55] D. S. Bouma, Z. Chen, B. Zhang, F. Bruni, M. E. Flatté, A. Ceballos, R. Streubel, L.-W. Wang, R. Q. Wu, and F. Hellman, Itinerant ferromagnetism and intrinsic anomalous Hall effect in amorphous iron-germanium, Phys. Rev. B **101**, 014402 (2020).

[56] R. Khasanov, D. Das, R. Gupta, C. Mielke, M. Elender, Q. Yin, Z. Tu, C. Gong, H. Lei, E. T. Ritz *et al.*, Time-reversal symmetry broken by charge order in CsV_3Sb_5, Phys. Rev. Res. **4**, 023244 (2022).

[57] M. H. Christensen, T. Birol, B. M. Andersen, and R. M. Fernandes, Loop currents in CsV_3Sb_5 kagome metals: Multipolar and toroidal magnetic orders, Phys. Rev. B **106**, 144504 (2022).

[58] T. Liang, J. Lin, Q. Gibson, S. Kushwaha, M. Liu, W. Wang, H. Xiong, J. A. Sobota, M. Hashimoto, P. S. Kirchmann *et al.*, Anomalous Hall effect in $ZrTe_5$, Nat. Phys. **14**, 451 (2018).

[59] S. Mozaffari, W. R. Meier, R. P. Madhogaria, N. Peshcherenko, S.-H. Kang, J. W. Villanova, H. W. S. Arachchige, G. Zheng, Y. Zhu, K.-W. Chen *et al.*, Universal sublinear resistivity in vanadium kagome materials hosting charge density waves, arXiv:2305.02393.

[60] G. Kresse and J. Furthmüller, Efficiency of *ab-initio* total energy calculations for metals and semiconductors using a plane-wave basis set, Comput. Mater. Sci. **6**, 15 (1996).

[61] G. Kresse and J. Furthmüller, Efficient iterative schemes for *ab initio* total-energy calculations using a plane-wave basis set, Phys. Rev. B **54**, 11169 (1996).

[62] P. E. Blöchl, Projector augmented-wave method, Phys. Rev. B **50**, 17953 (1994).

[63] J. P. Perdew, K. Burke, and M. Ernzerhof, Generalized gradient approximation made simple, Phys. Rev. Lett. **77**, 3865 (1996).

[64] V. Wang, N. Xu, J.-C. Liu, G. Tang, and W.-T. Geng, VASPKIT: A user-friendly interface facilitating high-throughput computing and analysis using VASP code, Comput. Phys. Commun. **267**, 108033 (2021).

[65] G. Pizzi, V. Vitale, R. Arita, S. Blügel, F. Freimuth, G. Géranton, M. Gibertini, D. Gresch, C. Johnson, T. Koretsune *et al.*, Wannier90 as a community code: New features and applications, J. Phys.: Condens. Matter **32**, 165902 (2020).